



Perylene imide supermolecule promote oxygen to superoxide radical for ultrafast photo-oxidation of 5-hydroxymethylfurfural

Yingxin Guo^a, Bing Liu^a, Jiawei Zhang^a, Guangli Wang^a, Chengsi Pan^a, Hui Zhao^a, Chuntao Wang^a, Feiyang Yu^a, Yuming Dong^{a,*}, Yongfa Zhu^{b,*}

^a International Joint Research Center for Photo-responsive Molecules and Materials, School of Chemical and Material Engineering, Jiangnan University, Wuxi 214122, China

^b Department of Chemistry, Tsinghua University, Beijing 100084, China

ARTICLE INFO

Keywords:

5-Hydroxymethylfurfural
Photocatalytic selective oxidation
Molecular oxygen reduction
Perylene imide supramolecular
Electron acceptor cocatalyst

ABSTRACT

The Photocatalytic preparation of 2, 5-diformylfuran (DFF) from biomass 5-hydroxymethylfurfural (HMF), is subjected to a low conversion efficiency. In view of superoxide radical is a crucial reactive oxygen species, we suggest an ultra-fast selective oxidation reaction achieved by modulating the photocatalytic oxygen reduction processes. Herein, we developed a novel photocatalytic system by anchoring perylene imide supramolecular as an oxygen reduction co-catalyst on ZnIn₂S₄. The functionalized perylene imide supramolecular as an active site greatly accelerates the generation of superoxide radical by absorbing oxygen while concentrating the photo-generated electrons of ZnIn₂S₄. Compared with pure ZnIn₂S₄, SA-PDI/ZnIn₂S₄ showed a more excellent photocatalytic performance under mild conditions (30-fold increase in photo-oxidation kinetics). Notably, the HMF transformation frequency is 1952 μmol·g⁻¹·h⁻¹, nearly one order of magnitude higher than previously reported techniques for photocatalytic HMF aerobic oxidation. This work open up a perspective for the design of photocatalytic systems for high added-value compounds production.

1. Introduction

5-Hydroxymethylfurfural (HMF) occupies an important position in chemical industry, which can be produced from carbohydrates with overproduction. Over the past decades, HMF has received tremendous attention for its widespread availability in value-added chemicals production [1,2], including 2, 5-diformylfuran (DFF), 2, 5-furandicarboxylic acid, 5-formyl-2-furancarboxylic acid and 5-hydroxymethyl-2-furancarboxylic acid [3–5]. Among them, DFF can be used in many spheres, such as Schiff bases, antimicrobial agents and conductor materials, and thus exhibit great economic values. However, DFF production by traditional chemical oxidation technology often leads to various risks and environmental issues for their high temperature and pressure reaction [6–9]. Therefore, developing an environmental-friendly catalytic system is of great significance for the oxidation of HMF into DFF [10]. As an efficient, safe and low-consumption oxidation approach, photocatalysis possesses several promising potentials for the value-added conversion of biomass-derived HMF.

Considerable research efforts have been devoted to photocatalysis DFF production, including C₃N₄-based composite [11,12], metallic oxide [13,14], and metal sulfide [15,16]. Recent experiments in this area suggested that ·O₂ play a cardinal role in photocatalysis selectively oxidizing HMF into DFF. Moreover, some problems that deserve to be noted and their solution are presented, such as in situ sensitization engineering, heterojunction strategy, and solvent effect to extend the ·O₂ lifetime and promote photogenerated charge separation. Great progress has been made in this field, but most of them are still limited because the neglect of the course of generating ·O₂ by reducing O₂. Therefore, the purpose of this work is to solve the issue for poor turnover frequency in photocatalytic transformation from HMF into DFF via stimulating the generation of ·O₂.

Among the available photocatalytic techniques, sulfide is a potential photocatalytic material [17]. As an excellent ternary sulfide based photocatalysts, ZnIn₂S₄ was suitable to construct a photocatalyst for selective oxidation of HMF benefitted from its suitable band edge positions and mild oxidation capacity [18]. However, the terminal atom of ZnIn₂S₄ is the saturated S atom [19,20], which is adverse to the

* Corresponding authors.

E-mail addresses: dongym@jiangnan.edu.cn (Y. Dong), zhuyf@tsinghua.edu.cn (Y. Zhu).

<https://doi.org/10.1016/j.apcatb.2023.123217>

Received 28 July 2023; Received in revised form 21 August 2023; Accepted 22 August 2023

Available online 24 August 2023

0926-3373/© 2023 Elsevier B.V. All rights reserved.

adsorption and further reduction of O_2 . Especially, the efficient selective-production of desired products has been restricted by the short of applicable co-catalyst to controllably reduce O_2 towards $\cdot O_2^-$. With respect to the foregoing, we assume the design and construction of a photocatalyst for reducing O_2 to promote $\cdot O_2^-$ generation can be anticipated. An ideal co-catalyst should meet the following conditions: a) Its electronic band structure can achieve oxygen reduction; b) Its energy level can match with $ZnIn_2S_4$; c) It can ensure intimate chemical contact with $ZnIn_2S_4$. Self-assembly perylene diimide supermolecule (SA-PDI) is a well-established organic photocatalytic material owing to its suitable energy band and excellent charge transfer capacity [21]. In addition, the connection between SA-PDI and other components can be changed by various modifications owing to its readily tunable monomer structure, which can drive the photogenerated electron transmission. As such, the integration of $ZnIn_2S_4$ with SA-PDI may meet the thermodynamic and kinetic requirements for the conversion of HMF to DFF.

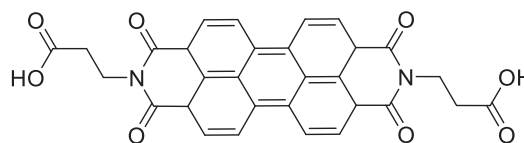
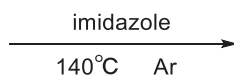
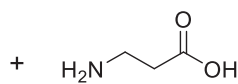
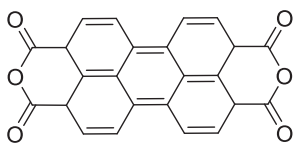
Herein, we innovatively selected a beta-alanine functionalized perylene imide supramolecule as a co-catalyst for the oxidation of HMF. Under mild conditions, the admirable yield of DFF was approximately 9.4 times higher than that of the original $ZnIn_2S_4$. In this study, the significantly enhanced kinetics in the photocatalytic HMF value-added transformation was credited to the superior oxophilicity and stronger electron-withdrawing properties of SA-PDI. What's more ingenious is that the coordination bond between SA-PDI and $ZnIn_2S_4$ will facilitate faster charge transfer and lead to higher photocatalytic performance. This work presents an original strategy for the environment-friendly selective oxidation of biomass-derived platform chemicals to value-added products.

2. Experimental sections

2.1. Materials and reagents

HMF and DFF were purchased from were purchased from Sinopharm Chemical Reagent Co. Ltd., Ltd. And indium nitrate tetrahydrate ($In(NO_3)_3 \cdot 4.5 H_2O$), cadmium nitrate tetrahydrate $Zn(NO_3)_2 \cdot 6 H_2O$, thioacetamide (TAA), Ethanol and other experimental reagents were purchased from Sinopharm Chemical Reagent Co., Ltd. All of the reagents were analytical grade without further purification. Deionized water was used throughout this study.

2.2. Synthesis of self-assembled PDI (SA-PDI)



Perylene diimide (PDI) was synthesized by following previous work [22]. First, 1.37 g 3,4,9,10-perylenetetrahydride (PDTH), 2.49 g β -alanine and 18 g imidazole were heated at 140 °C for 6 h under an argon atmosphere. Afterwards, the reactant was washed with 100 mL ethanol and 300 mL 2 M HCl. Then, PDI was obtained by washing with distilled water and dried under vacuum at 60 °C for 8 h. Subsequently, 0.4 g of PDI was dispersed in 200 mL ultrapure water and added 830 μ L triethylamine solution with constantly stirring. The solution was magnetically stirred for 10 min. Subsequently, 30 mL 4 M HCl was added while stirring for 30 min. The sample was centrifuged and washed till neutral and dried under vacuum at 60 °C for 8 h. The obtained samples was denoted as SA-PDI.

2.3. Synthesis of SA-PDI / $ZnIn_2S_4$ composites

0.2 mmol $Zn(NO_3)_2 \cdot 6H_2O$, 0.4 mmol $In(NO_3)_3 \cdot 4.5H_2O$ and 0.8 mmol TAA were dissolved in 50 mL of deionized water, and stirred continuously for half an hour. And then, different amounts of PDI were added to the above solutions and mixed evenly. The obtained mixture was heated at 60 °C in an oil bath under stirring for 8 h. After reaction finished, the suspension was centrifuged to separate the solid catalyst. Subsequently, the collected solid was washed with water and ethanol for three times, and then dried at 60 °C for 4 h (Scheme S1). The obtained samples are denoted as 0.5 wt% P/Z, 1 wt% P/Z, 1.5 wt% P/Z, 5 wt% P/Z, and 50 wt% P/Z, respectively, according to the PDI content. For comparison, pure $ZnIn_2S_4$ (ZIS) nano sheets were synthesized under the same reaction conditions without the addition of SA-PDI. In addition, the physically mixed composites were prepared by mechanical grinding in the same proportion.

2.4. Sample characterization

The composition and crystallinity of the catalyst were determined by the 2 θ scanning range 5–90° X-ray diffractometer (XRD, Cu K α , Bruker AXS Co., Germany,) for analysis. The total reflection Fourier infrared spectrometer (FT-IR, Nicolet 6700, Bruker AXS Co., Germany) determines the chemical functional group structure of the photocatalyst. Transmission electron microscopy (TEM) and high resolution transmission electron microscopy (HRTEM) images were collected on a JEM-2100 plus transmission electron microscope (JEOL, Japan) to examine the morphology and size of sample. To detect surface species of sample, X-ray photoelectron spectroscopy (XPS) analysis was conducted using an ESCALAB 250 Xi (ThermoFisher, America) X-ray photoelectron spectrometer with Al K α line as the excitation source ($h\nu = 1484.8$ eV) and adventitious carbon (284.8 eV for binding energy) was used as reference to correct the binding energy of sample. UV–vis diffuse reflectance spectra were measured on a UV-3600 (Shimadzu, Japan) spectrophotometer. Fluorescence spectrometer with an excitation wavelength of 375 nm and ultrafast time-resolved fluorescence spectrometer (TRFLS, Lifespec II) were used to measure the characteristics of photogenerated carriers. Zeta potential was analyzed by ZetaPALS. Nuclear magnetic resonance (NMR) was measured by BRUKER AVANCE 400. Electron spin resonance (ESR) signals of spin-trapped paramagnetic species with 5, 5-dimethyl-1-pyrroline-N-oxide (DMPO) were detected using a Bruker A300E spectrometer (Bruker AXS Co., Germany). The components of products in the reaction system were analyzed by LC-

U3000 (Shimadzu, Japan). The electrochemical workstation (CHI 660D, Shanghai Chenhua Instruments Co., Ltd.) was used to measure the EIS Nyquist spectrum, and Mott Schottky curve of the photocatalyst, and the transient photocurrent was measured under the conditions of a 300 W xenon lamp. And surface photovoltage (SPV) was measured by homemade equipment.

2.5. Photocatalytic HMF conversion measurements

In a typical run, 2.6 mg HMF and 10 mL CH_3CN were charged into a 25 mL quartz flask with a magnetic stirring at the speed of 800 rpm. The SA-PDI /ZIS catalyst (20 mg) was then dispersed into the reactant solution, oxygen was passed for 30 min, and then the reaction was carried

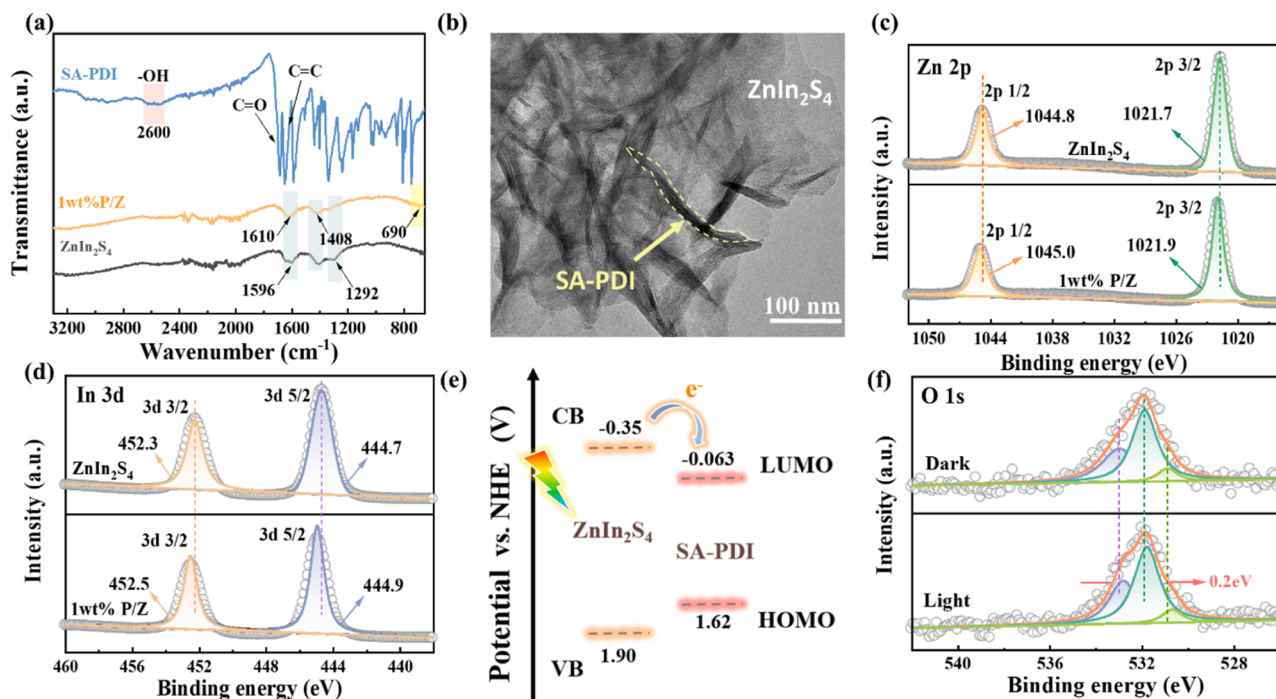


Fig. 1. (a) FT-IR of ZnIn₂S₄, PDI and 1 wt%SA-PDI/ZnIn₂S₄ samples, (b) HAADF-STEM images of the 1wt% SA-PDI/ZnIn₂S₄ catalyst, (c-d) High-resolution XPS spectra of Zn and In in the 1 wt%SA-PDI /ZnIn₂S₄ sample, (e) Schematic energy-level diagram of SA-PDI and ZnIn₂S₄, (f) O 1 s XPS spectra for 1 wt%SA-PDI/ZnIn₂S₄ under dark and light irradiation.

out under a 300 W xenon lamp. After the reaction, the supernatant was collected by centrifugation and analyzed using HPLC-U3000.

The selectivity and conversion of HMF to DFF were calculated according to the following formula [23]:

$$\text{Conversion } (\%) = 100 \times \frac{C_{\text{HMF}}^{\text{initial}} - C_{\text{HMF}}^{\text{final}}}{C_{\text{HMF}}^{\text{initial}}} \quad (1)$$

$$\text{Selectivity } (\%) = 100 \times \frac{C_{\text{DFF}}}{C_{\text{HMF}}^{\text{initial}} - C_{\text{HMF}}^{\text{final}}} \quad (2)$$

$$\text{Yield } (\%) = 100 \times \frac{C_{\text{DFF}}}{C_{\text{HMF}}^{\text{initial}}} \quad (3)$$

$$\text{TOF} = \frac{\text{moles}_{\text{HMF}}^{\text{initial}} (\mu\text{mol}) * \text{Conversion}_{\text{HMF}}}{m_{\text{cat.}} (\text{g}) * \text{Time} (\text{s})} \quad (4)$$

In order to further understand the photocatalytic mechanism of SA-PDI/ZnIn₂S₄, in same reaction conditions, different sacrificial agents (10 mmol/L) were added for trapping experiments, such as Mn(OAc)₂ as electron scavenger, benzoquinone(BQ) as ·O₂ scavenger, Na₂-EDTA as hole scavenger and isopropanol (IPA) as ·OH scavenger.

2.6. Calculation details

All the spin-polarized density functional theory (DFT) calculations were performed by using the Vienna ab initio simulation package (VASP) [24,25]. The D3 correction method (DFT-D3) was employed in order to include van der Waals (vdW) interactions [26]. The projector-augmented wave (PAW) method was used to represent core-valence interactions [27]. Valence electrons were described by a plane wave basis with an energy cutoff of 400 eV. The generalized gradient approximation with the Perdew-Burke-Ernzerhof (GGA-PBE) functional was used to model electronic exchange and correlation [28]. Electron smearing was employed via Gaussian smearing method with a smearing width consistent to 0.05 eV. The conjugate gradient algorithm was used in geometry optimization calculations. Optimized structures

were obtained by minimizing the forces on each ion until they were less than 0.03 eV/Å. The energy convergence criteria was set to 10⁻⁵ eV. The Brillouin zone was sampled at the 3 × 3 × 1 k-point mesh. The adsorption energy (E_{ads}) is defined as follows.

$$E_{\text{ads}} = E_{\text{adsorbate/substrate}} - E_{\text{adsorbate}} - E_{\text{substrate}}$$

Where E_{adsorbate/surface}, E_{adsorbate} and E_{substrate} represent the energies of substrate with the adsorbate species, the adsorbate molecule, and the substrate, respectively. A negative value means the process is exothermic adsorption. Charge distributions were analyzed with Bader's model (Fig. S1-S2).

3. Results and discussion

3.1. Structural characterization of SA-PDI/ ZnIn₂S₄ catalyst

The SA-PDI/ZnIn₂S₄ composite were fabricated by in-situ loading the SA-PDIs onto the preformed ZnIn₂S₄ solutions (Scheme S1). After the one-pot reaction, characteristic peaks of carboxylic O-H stretching in SA-PDI/ZnIn₂S₄ (2600 cm⁻¹) were not detected (Fig. 1a & S3). The FTIR spectra of different proportions of SA-PDI/ ZnIn₂S₄ show similar peaks around 1600 and 1400 cm⁻¹, respectively, which be ascribed to the M-S bond [29–31]. The vibrational bands of 1292 cm⁻¹ and 1408 cm⁻¹ emerged in ZnIn₂S₄ are obviously weaker than SA-PDI/ZnIn₂S₄, which are affected by the interaction between metal atoms and the carboxyl group of SA-PDI. New peaks appeared at 690 cm⁻¹ for SA-PDI /ZnIn₂S₄, corresponding to the Metal-Oxygen bond stretching in the carboxy group. The spectroscopic data supported the formation of coordination bonds via one-pot method. The assignment was corroborated by X-ray diffraction (XRD) (Fig. S4). The EDX elemental mapping analysis of the SA-PDI/ZnIn₂S₄ sample reveal that the three characteristic elements of C, N and O are evenly distribution in the ZnIn₂S₄ (Fig. S5). The morphology of SA-PDI/ZnIn₂S₄ catalyst was characterized afterward. As displayed in Fig. 1b, the TEM images revealed that the synthesized SA-PDI is fibrous in shape with a diameter of 10 nm and a length of 400 nm, and can be intuitively observed in the TEM diagram of the

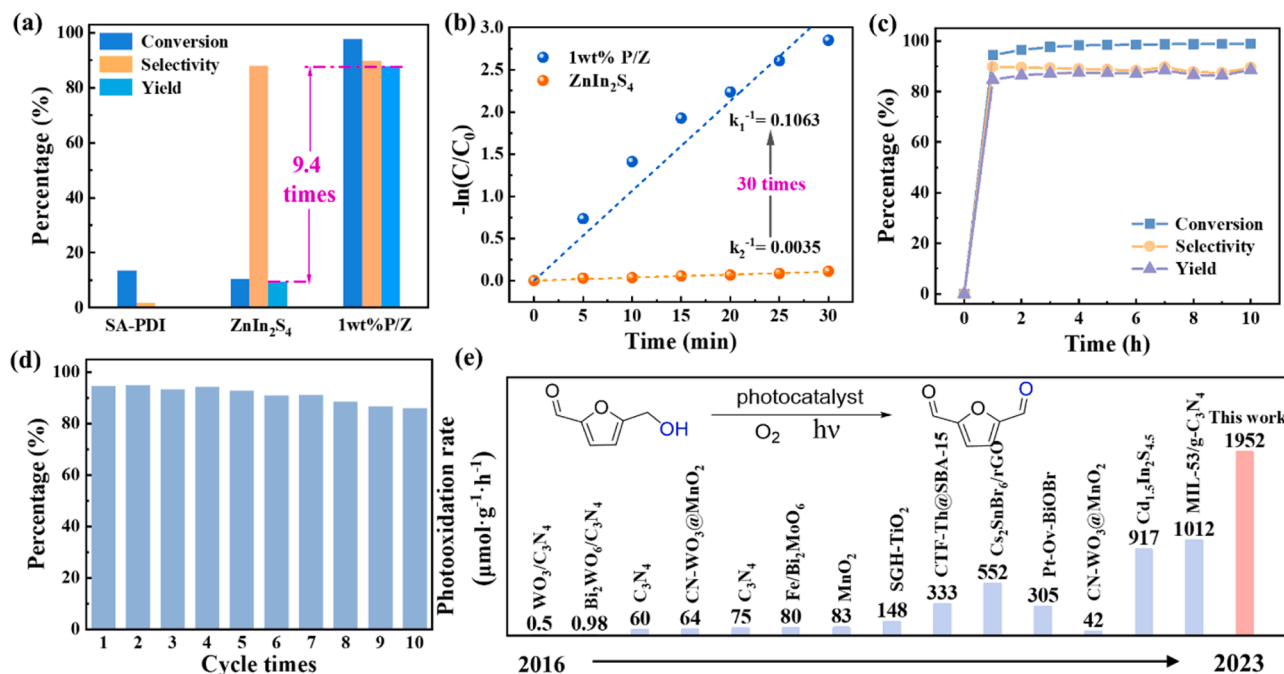


Fig. 2. (a) Comparison of photocatalytic oxidation of HMF in O₂ on different samples (reaction time 0.5 h), (b) First order kinetic curve of different samples, (c) Oxidation rate of HMF by 1 wt% SA-PDI /ZnIn₂S₄ in 10 h, (d) Stability test for 1 wt% SA-PDI/ZnIn₂S₄ sample, (e) Comparison of recently reported results HMF oxidation to DFF results with other photocatalysts under O₂ conditions.

composite [32,33]. Fig. 1b and S6 indicated that SA-PDI particles were evenly anchored on the ZnIn₂S₄. Brunauer-Emmett-Teller (BET) surface areas for 1 %wt SA-PDI/ZnIn₂S₄ was calculated to be 98 m² g⁻¹. This result also means that the SA-PDI is effectively anchored to the ZnIn₂S₄'s surface, (Fig. S7). Coordinate bond between SA-PDI and ZnIn₂S₄ in the catalyst should be attributed to SA-PDI with hydrophilic, which increase the molecular collision dynamics between SA-PDI and inorganic metal particles [34]. On the other hand, the surface of the SA-PDI is negatively charged, and favorable for positively charged metal ions (Zn²⁺ and In²⁺) to adsorb to SA-PDI via electrostatic interactions and further bond with the carboxyl group [35–37] (Fig. S8). The survey X-ray photoelectron spectra (XPS) of SA-PDI/ZnIn₂S₄ showed the presence of C, N, O, Zn, In and S (Fig. S9). Fig. 1c exhibited the high-resolution Zn 2p and In 3d XPS peaks being assigned to ZnIn₂S₄ and SA-PDI/ZnIn₂S₄. Compared with pure ZnIn₂S₄, the Zn 2p and In 3d peaks position of SA-PDI/ZnIn₂S₄ are shifted toward low binding energy, revealing a strong interaction between ZnIn₂S₄ and SA-PDI. The S 2p spectrum for ZnIn₂S₄ separately displays two peaks at 161.3 and 162.4 eV. After loading SA-PDI, a red-shift of ~0.2 eV in 1 wt% PDI/ZIS is observed, demonstrating that the electrons in Zn-S and In-S are transferred to Zn-O and In-O bonds [38–41] (Fig. S10).

In the chemical connection between two components, the bonding bridge constructed by the hybrid orbital is very conducive to intermolecular charge transfer [42]. In contrast, in XPS of the physical mixture of SA-PDI and ZnIn₂S₄, the binding energy of each element is consistent with the pure SA-PDI and ZnIn₂S₄, respectively (Fig. S11), meaning the cause of the surface chemical reaction is hardly produced among mixtures. These results indicate that, as expected, the coordinate covalent bond is formed between ZnIn₂S₄ and the co-catalyst SA-PDI. The band gaps (E_g) of SA-PDI and ZnIn₂S₄ were estimated to be about 1.69 eV and 2.26 eV, respectively, which from UV–vis spectra and the corresponding Tauc plots (Figs. S12). Fig. 1e and Fig. S13–14 demonstrated that the lowest unoccupied molecular orbital (LUMO) energy level of SA-PDI is about -0.063 V (vs. NHE), which is significantly lower than the conduction band (CB) edge level of the ZnIn₂S₄ (about -0.350 V vs. NHE). Under the circumstances, the photo-generated electrons in ZnIn₂S₄ can preferentially transferred to SA-PDI after their connection and enriched

on its surface, as evidenced by the XPS under illumination (Fig. 1f). Compared with original ZnIn₂S₄, the binding energy of O 1s in SA-PDI/ZnIn₂S₄ composites decreases by about 0.2 eV upon light irradiation, and the Zn, In and S peaks were shifted to high energy accordingly (Fig. S15). The above experimental data declare the successful construction of the composites and the close connection between SA-PDI and ZnIn₂S₄. Moreover, as we designed, as an electron acceptor, SA-PDI's energy level and that of ZnIn₂S₄ are perfectly matched.

3.2. Highly efficient HMF conversion of SA-PDI/ ZnIn₂S₄ photocatalyst

After confirming the expected structure, the selective oxidation HMF results of SA-PDI, ZnIn₂S₄ and 1 wt% P/Z on HMF were devoted to evaluate the improvement of photocatalytic performance of the co-catalyst SA-PDI. As depicted in Fig. 2a, both SA-PDI and ZnIn₂S₄ can not be qualified to the efficient preparation of DFF, but a series of samples with different composite ratios exhibited varying degrees of performance enhancement of photocatalytic oxidize HMF (Fig. S16). In particular, the 1 wt% PDI/ZIS composite displayed an extremely high oxidation rate (1952 μmol g⁻¹ h⁻¹), achieving up to 97.7 % conversion of HMF after only 0.5 h, while maintaining an excellent selectivity of 89.8 % for DFF. Additionally, the obviously difference HMF oxidation rates in various atmospheres (nitrogen, air, and oxygen), revealing O₂ is featured on photocatalytic oxidation process of HMF (Fig. S17). Interestingly, 1 wt% P/Z composites showed excellent activity for HMF conversion and DFF selectivity of 97.3 % and 95.7 %, respectively, after extending illumination time to 3 h. On the contrary, it's worth noting that the mixtures consisted of original ZnIn₂S₄ and SA-PDI could hardly be applied for HMF conversion under uniform reaction conditions (Fig. S18). The light-driven transformation efficiency of HMF at 1 wt% P/Z was presented via the kinetic model. SA-PDI significantly improved the oxidation rate of HMF with the rate constant k_1 30 times higher than ZnIn₂S₄ (k_2) (Fig. 2b). Thus, incorporation into SA-PDI significantly improved the kinetics of carriers from ZnIn₂S₄.

Moreover, the over-oxidation of DFF was negligible within 10 h of irradiation, which can be up to the requirement of selectively produced DFF (Fig. 2c). Catalyst recyclability is of paramount importance, even

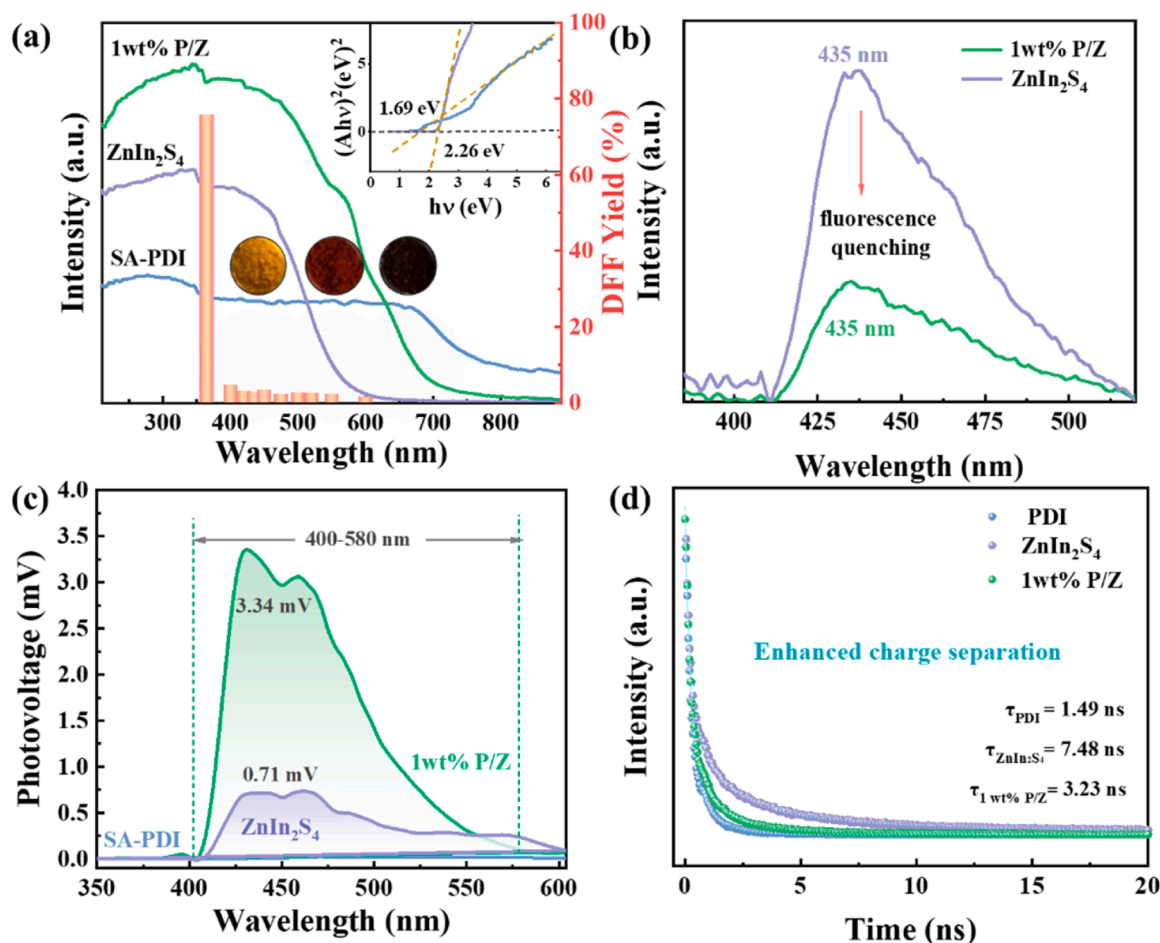


Fig. 3. (a) Wavelength dependence of DFF yield for 1 wt% PDI/ ZnIn₂S₄ sample, (b) Steady-state PL spectra, (c) Surface photovoltage and (d) Time-resolved PL spectra of synthesized photocatalysts.

more so for practical applications. In Fig. 2d, HMF conversion is nearly identical from 1st to 10th runs. Further analysis of the XRD patterns of the catalysts before and after the reaction (Fig. S19) indicated that the crystal structure of SA-PDI/ZnIn₂S₄ hardly changed during the reaction.

As mentioned above, SA-PDI co-catalyst can not only effectively promote DFF generation, but also has good reaction stability. Furthermore, the catalytic activity of 1 wt%SA-PDI/ZnIn₂S₄ (1 wt% P/Z) was 9.4-fold higher than primary ZnIn₂S₄, confirming the key role of SA-PDI co-catalyst. We investigated the performance of 1 wt%SA-PDI/ZnIn₂S₄ on HMF conversion to DFF and compared it with those of reported photocatalytic techniques, including some noble metal-based photocatalysts. The data in Fig. 2e and Table S1 shown that 1 wt% P/Z gives a record-high catalytic activity in HMF selective oxidation. Among the most of catalytic systems for HMF oxidation, superoxide radicals are highly effective in promoting the formation of DFF, that is precisely the slowest step among these quential and parallel oxidation steps [43]. Therefore, rapidly generating abundant $\cdot\text{O}_2^-$ in situ is a powerful strategy for the photocatalytic targeted oxidation of HMF to DFF [44–46]. In light of the excellent properties of SA-PDI, we envisage that it could be a desirable co-catalyst for the reduction molecular oxygen to produce $\cdot\text{O}_2^-$.

3.3. Excellent electron extraction of SA-PDI for O₂ reduction

The comparison among UV–vis spectra of SA-PDI, ZnIn₂S₄ and 1 wt% PDI/ZIS showed that the absorption peaks of the 1 wt%PDI/ZIS catalyst are mainly derive from ZnIn₂S₄. Furthermore, the absorption intensity of the 1 wt%PDI/ZIS catalyst is stronger than those of the corresponding bands of ZnIn₂S₄. The changes in absorption bands are attributed to the

strong interaction between SA-PDI and ZnIn₂S₄, suggesting that SA-PDI co-catalyst were firmly bonded on the surface of ZnIn₂S₄ [47]. Notably, the broad characteristic absorption peak at ~ 700 nm from SA-PDI show no signs in the spectrum of the 1 wt%PDI/ZIS catalyst (Fig. 3a). The wavelength dependence results also showed an excellent DFF yield of 75.8 % at 365 ± 5 nm. However, at 600 ± 5 nm, the HMF conversion was only 1.6 %. These results indicated that the light absorption of SA-PDI is inoperative to induce the reaction, and the HMF oxidation activity was mainly excited by absorption wavelength of ZnIn₂S₄. This is a critical evidence to suggest that SA-PDI did not play a major role in photo-absorption but functioned as a co-catalyst in photocatalytic system. Furthermore, photoluminescence (PL) was conducted to investigate the SA-PDI co-catalytic behaviors. As shown in Fig. 3b, under 375 nm excitation, both ZnIn₂S₄ and 1 wt%PDI/ZIS exhibited the maximum emission peak at 435 nm, which was assigned to the characteristic emission of ZnIn₂S₄. Additionally, the fluorescence intensity of 1 wt%PDI/ZIS is significantly quenched compared with ZnIn₂S₄. Surface Photovoltaic spectra (SPV) of SA-PDI, ZnIn₂S₄ and 1 wt%PDI/ZnIn₂S₄ was further measured to gain a more comprehensive understanding of the characteristics of SA-PDI co-catalyst. The results, as shown in Fig. 3c, demonstrate that after anchoring the SA-PDI co-catalyst onto the surface of ZnIn₂S₄, there is a significant enhancement in responses within the 400–580 nm range. This delivers significantly better charge separation efficiency can be attributed to the excellent electron extraction capability of SA-PDI and its covalent connection with ZnIn₂S₄. In contrast to these findings, no SPV response was observed for SA-PDI within this wavelength range. We speculate that this might be due to the photo-generated electrons of SA-PDI are not sufficient to be excited in this

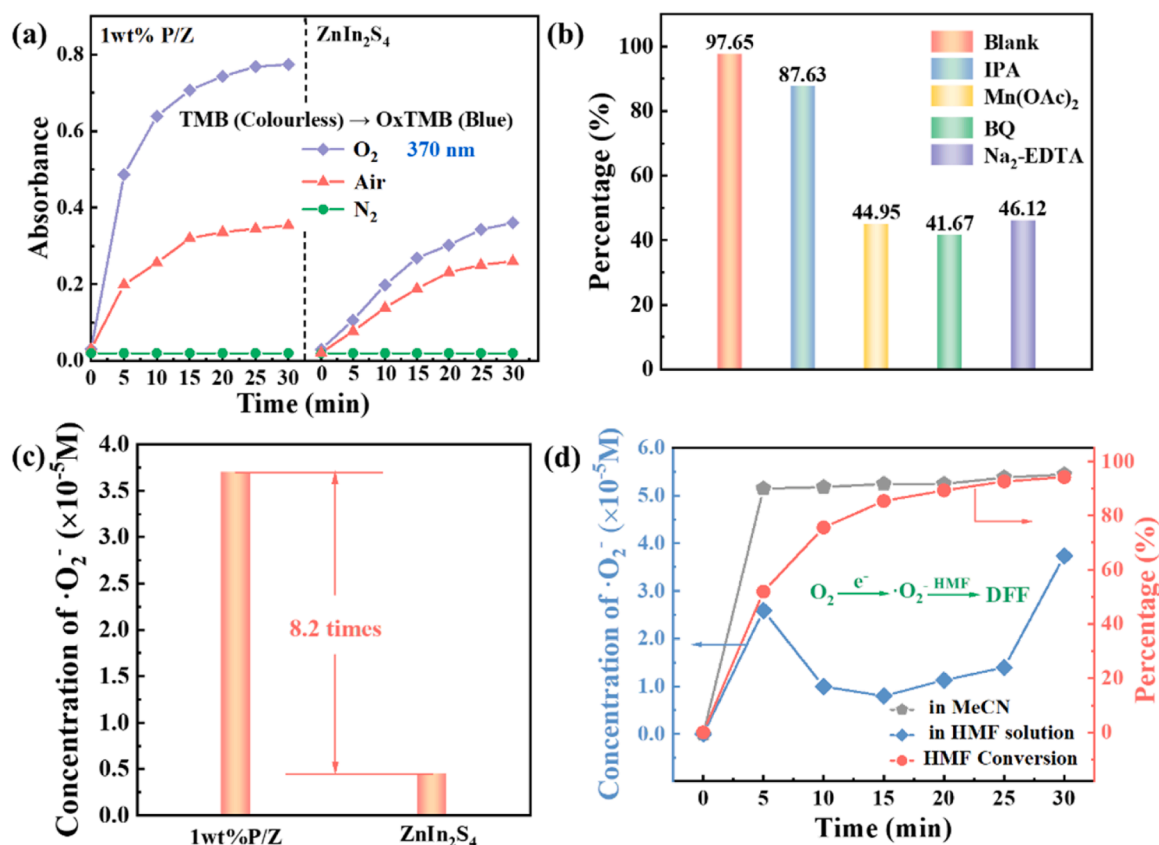


Fig. 4. (a) The absorbance peak monitored for the product at 370 nm vs reaction time under different gas conditions, (b) The species trapping experiments for oxidation of HMF to DFF, (c) Photocatalytic generation of $\cdot\text{O}_2^-$ for 1 wt% SA-PDI/ZnIn₂S₄ and ZnIn₂S₄ by NBT method, (d) Concentration dependence of $\cdot\text{O}_2^-$ for photocatalytic HMF oxidation in O₂.

wavelength range. The result now provides a cogent evidence to SA-PDI playing a co-catalyst role in the process of HMF transformation catalyzed by 1 wt%PDI/ZnIn₂S₄ composite photocatalyst. Likewise, time-resolved PL spectroscopy revealed the property of the photo-generated carriers in the sample (Fig. 3d.). According to calculations, the average PL lifetime of the sample decreases from 7.48 ns to 3.23 ns, after SA-PDI co-catalyst was introduced into the system. In general, the shorter the average PL duration, the greater the effect of charge carrier splitting. These conclusions were further supported by electrochemical impedance spectroscopy (EIS) measurements (Fig. S20).

To demonstrate the favorable role of co-catalyst in O₂ reduction, we performed the O₂ activation experiments taking 3, 3', 5, 5'-tetramethylbenzidine (TMB) as the indicator (Fig. 4a & S21) [48]. The significant difference of TMB oxidation rates in various gas environments (O₂, air, and N₂) indicated that $\cdot\text{O}_2^-$ arose from O₂ reduction. It can be sure that the augmented O₂ reduction ability is attributed to co-catalyst. In order to further reveal the O₂ reduction mechanism on the co-catalyst SA-PDI, isopropyl alcohol (IPA), Mn(OAc)₂, Na₂-EDTA and p-benzoquinone (BQ) were added into the reaction system aiming to specifically inhibit the generation of $\cdot\text{OH}$, e^- , h^+ and $\cdot\text{O}_2^-$, respectively (Fig. 4b). As we expected, $\cdot\text{OH}$ barely played a role in the reaction process (HMF conversion rate 87.63 %) and BQ dramatically decreased HMF oxidation (41.67 %), which indicated that $\cdot\text{O}_2^-$ is the primary photo-generated ROS. In addition, the reaction activity decreased to 44.95 % after electrons were captured via Mn(OAc)₂, which was very close to the catalytic activity after inhibiting $\cdot\text{O}_2^-$, indicating that the electrons mainly used to reduce O₂ to $\cdot\text{O}_2^-$ under photoexcitation. The signal peak of SA-PDI/ZnIn₂S₄ is much more pronounced in contrast with ZnIn₂S₄, showing SA-PDI co-catalyst is propitious to reduce O₂ into $\cdot\text{O}_2^-$ through electron transfer, which is in line with the photocatalytic performance of the

samples.

Electron paramagnetic resonance (EPR) spectroscopy using 5, 5-dimethyl-1-pyrroline N-oxide (DMPO) as the spin-trap was applied in order to identify the active oxygen species, and $\cdot\text{O}_2^-$ signal was clearly observed when the experiment was conducted with illumination (Fig. S22). Molecular oxygen was reduced and generated $\cdot\text{O}_2^-$ by accepting electron from SA-PDI LUMO. And the concentration of $\cdot\text{O}_2^-$ can be quantified by its specific reaction with nitro blue tetrazolium (NBT) [49]. As illustrated in Fig. 4c, the data suggests an 8-fold promotion of the $\cdot\text{O}_2^-$ concentration of PDI/ZnIn₂S₄ relative to that of original ZnIn₂S₄. From these data, the electron concentration of 1 wt% PDI/ZnIn₂S₄ was estimated to be 8 times that of ZnIn₂S₄, and was consistent with the photocatalytic performance. Benefiting from the enhanced O₂-reduction ability, $\cdot\text{O}_2^-$ free radical was rapidly generated and their concentration reached the maximum within 5 min. Meanwhile, the selectivity of DFF also peaked over 99 %. Compared with the condition without substrate, the selectivity of DFF also decreased with the consumption of $\cdot\text{O}_2^-$ (Fig. 4d). After 30 min light irradiation, $\cdot\text{O}_2^-$ no longer participated in the reaction oxidation of HMF and accumulated to the initial concentration, which was consistent with the results of the activity test in the reaction (Figure.S23). With the production of concentrated $\cdot\text{O}_2^-$, a large number of photo-generated electrons was consumed, which should greatly affect the charge carrier separation process [50,51]. Above results indicate that strong interaction between the two work as an electron bridge and provide more convenience for oxygen reduction reaction and the generation of $\cdot\text{O}_2^-$. Remarkably, molecular oxygen adsorption is necessary to improve the generation efficiency of superoxide radical anion. The type and intensity of molecular oxygen adsorption on SA-PDI/ZnIn₂S₄ and ZnIn₂S₄ surfaces were investigated by temperature programmed desorption (TPD) [52].

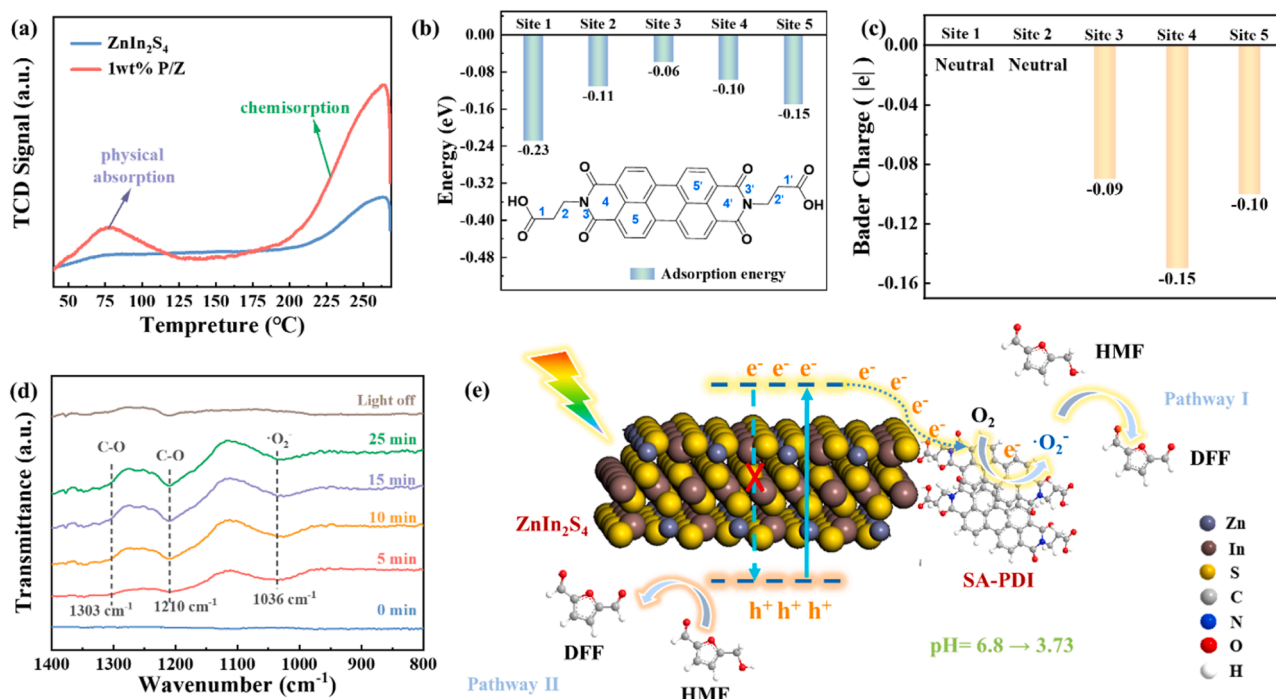


Fig. 5. (a) O₂-TPD spectra of 1 wt%PDI/ZnIn₂S₄ and ZnIn₂S₄, (b) Calculated oxygen adsorption energies on different sites of SA-PDI. (c) Bader charge analysis of oxygen on different sites of SA-PDI. (d) In situ FT-IR spectra for the photocatalytic system of SA-PDI/ZnIn₂S₄. (e) Tentative mechanism of the photocatalysis oxidation process with SA-PDI /ZIS.

3.4. Efficient adsorption of O₂ on SA-PDI for generation of ·O₂

As shown in Fig. 5a, there are two types of O₂ adsorbed species on the SA-PDI/ZnIn₂S₄ and ZnIn₂S₄ surfaces. The peak intensity of SA-PDI/ZnIn₂S₄ at about 75 °C corresponding to O₂ physical adsorption is slightly higher than that of ZnIn₂S₄. However, the peak at 250 °C, related to the chemisorption of O₂, is much stronger than that of ZnIn₂S₄. This evidence indicates the SA-PDI/ZIS has a better affinity to O₂ molecules, which can contribute to the reduction step in photocatalysis. The similar results in high-resolution O 1s XPS spectrum (Fig. S24). It is demonstrated that the ratio of adsorbed oxygen in SA-PDI/ZnIn₂S₄ composite is significantly higher than that of original ZnIn₂S₄. The stronger oxygen affinity of the co-catalyst indicates a greater possibility of oxygen reduction reactions on its surface. In order to gain deeper insight into the oxygen affinity of SA-PDI, the density functional theory (DFT) calculations were performed with molecular models. In Fig. 5b, the oxygen adsorption energies on the different sites on the surface of SA-PDI are calculated to be less than zero, demonstrating the multi-site nature of SA-PDI co-catalyst for O₂ reduction. The superoxide radical formation pathway on SA-PDI corresponds to the accepting electron process of molecular oxygen. Moreover, DFT calculations were then carried out to investigate the charge transfer between different sites of SA-PDI and molecular oxygen. According to the results in Fig. 5c, some electrons which in site 3–5 can be transfer to varying degrees to molecular oxygen, suggesting the C atoms in the benzene ring exhibit favorable electron transfer capacity to form the ·O₂ compared to other possible sites. Thus, the C atoms in benzene ring of SA-PDI co-catalyst most likely serve as the active sites for photocatalytic O₂ reduction [53]. Details of Bader analysis are provided in the Fig. S25.

The production of reactive oxygen species during the oxygen reduction process predicted by DFT calculations were further confirmed by means of in situ DRIFTS spectrometry. As exhibited in Fig. 5d and S26, the peaks at 900–971 cm⁻¹ are observed, being assigned to the O-O stretching vibration of adsorbed oxygen on bare ZnIn₂S₄. For SA-PDI/ZnIn₂S₄ this is different, the characteristic peaks of O-O at 900–971 cm⁻¹ has obviously disappeared. The C-O stretching vibration

band at 1200–1310 cm⁻¹ after irradiation confirms the formation of C-O-O-C* intermediate species in benzene ring, revealing SA-PDI is the only oxygen-reduction component of SA-PDI/ZnIn₂S₄ during the photocatalytic process. In addition, in pace with the irradiation time increasing, the intensity of the signals at 1036 cm⁻¹ attributed to ·O₂ is gradually ascending, indicating the formation of ·O₂ from O₂ in the photocatalytic system of SA-PDI/ZnIn₂S₄ [54,55]. As we predicted, using β-alanine functionalized perylene imide supermolecule as a co-catalyst can extract photogenerated charge carriers from ZnIn₂S₄ and facilitate reduction adsorbed O₂ into ·O₂ with soft oxidizing capacity by electron transfer processes [56], solving the bottleneck problem of poor HMF oxidation efficiency. By analyzing the above experimental results, a credible mechanism was proposed to illustrate the photo-oxidation of HMF by 1 wt%PDI/ZIS. Owing the matching band structure, the photo-generated e⁻ and h⁺ separated efficiently at the SA-PDI and ZnIn₂S₄ interface, respectively. Then, the photo-generated electron migrated from ZnIn₂S₄ (CB) to SA-PDI (LUMO), and O₂ adsorbed on the surface of SA-PDI capture electrons and convert to superoxide-radicals. At the same time, HMF is preliminarily oxidized to active-intermediates by the timely photo-generated holes. Afterwards, the formed ·O₂ will oxidize the carbon-centered radicals into the target DFF products on 1 wt%PDI/ZIS (Fig. 5e). SA-PDI competently extracts photogenic electron from ZnIn₂S₄ and efficiently reduce O₂ to ·O₂, due to the intense interaction between SA-PDI and ZnIn₂S₄. Apart from photo-generated electron, the hole are also efficiently utilized. This is owing to photoelectrons was consumed to the production of ·O₂, the recombination of photogenerated charge carriers is significantly inhibited. Therefore, the ultra-efficient selective oxidation of HMF was achieved.

4. Conclusion

In conclusion, we have successfully developed a highly promising photocatalyst for ultrafast selective oxidation of HMF, via anchoring SA-PDI onto ZnIn₂S₄. The crucial factor in generating reactive oxygen species lies in the directional transmission of photo-generated electrons to chemisorbed molecular oxygen. Owing to the specific affinity for

molecular oxygen, the co-catalyst provides a favorable platform for the adsorption of molecular oxygen. More importantly, based on their matching energy band structure, co-catalyst acts as an electron concentrator and can gather the photogenic electrons from ZnIn₂S₄ for the reduction of adsorbed molecular oxygen. In particular, the coordination bond formed between the two can be used as a bridge to shorten the transport path of photogenerated electrons and accelerate the supply of electrons for oxygen reduction. All of these provide a unique reaction environment rich in O₂ species, which is highly favorable for selective oxidation of organic compounds. The construction of supramolecular electron acceptor co-catalyst and its functionalities will provide a universal strategy for O₂-participating photocatalytic reactions.

CRedit authorship contribution statement

Y.X. Guo, J.W. Zhang, H. Zhao, Y.M. Dong and Y.F. Zhu for Data curation, Formal analysis and draft writing of materials and photocatalytic performance. Y.X. Guo, C.S. Pan, J.W. Zhang, G.L. Wang, C.T. Wang, F.Y. Yu, Y.M. Dong and Y.F. Zhu for Data curation and Formal analysis and draft writing of charge separation/transfer kinetics. Y.X. Guo, B. Liu, Y.M. Dong and Y.F. Zhu for Data curation and Formal analysis and draft writing of the first-principle calculation based on the Density Functional Theory.

Declaration of Competing Interest

The authors declare that they have no known competing financial interests or personal relationships that could have appeared to influence the work reported in this paper.

Data Availability

Data will be made available on request.

Acknowledgements

The work is supported by the National Natural Science Foundation of China (22172064, 22136002).

Appendix A. Supporting information

Supplementary data associated with this article can be found in the online version at doi:10.1016/j.apcatb.2023.123217.

References

- [1] F. Wang, H. Duan, Opportunities and future directions for photocatalytic biomass conversion to value-added chemicals, *Chem. Catal.* 2 (2022) 644–646.
- [2] S. Shylesh, A.A. Gokhale, C.R. Ho, A.T. Bell, Novel strategies for the production of fuels, lubricants, and chemicals from biomass, *Acc. Chem. Res.* 50 (2017) 2589–2597.
- [3] S. Xu, P. Zhou, Z. Zhang, C. Yang, B. Zhang, K. Deng, S. Bottle, H. Zhu, Selective oxidation of 5-hydroxymethylfurfural to 2,5-furandicarboxylic acid using O₂ and a photocatalyst of Co-thiophenopyrazine bonded to g-C₃N₄, *J. Am. Chem. Soc.* 139 (2017) 14775–14782.
- [4] J.N. Chang, Q. Li, Y. Yan, J.W. Shi, J. Zhou, M. Lu, M. Zhang, H.M. Ding, Y. Chen, S.L. Li, Y.Q. Lan, Covalent-bonding oxidation group and titanium cluster to synthesize a porous crystalline catalyst for selective photo-oxidation biomass valorization, *Angew. Chem. Int. Ed.* 61 (2022), e202209289.
- [5] G. Wang, R. Huang, J. Zhang, J. Mao, D. Wang, Y. Li, Synergistic modulation of the separation of photo-generated carriers via engineering of dual atomic sites for promoting photocatalytic performance, *Adv. Mater.* 33 (2021), e2105904.
- [6] X. Huang, O. Akdim, M. Douthwaite, K. Wang, L. Zhao, R.J. Lewis, S. Pattison, I. T. Daniel, P.J. Miedziak, G. Shaw, D.J. Morgan, S.M. Althabhan, T.E. Davies, Q. He, F. Wang, J. Fu, D. Bethell, S. McIntosh, C.J. Kiely, G.J. Hutchings, Au–Pd separation enhances bimetallic catalysis of alcohol oxidation, *Nature* 603 (2022) 271–275.
- [7] E. Hayashi, Y. Yamaguchi, K. Kamata, N. Tsunoda, Y. Kumagai, F. Oba, M. Hara, Effect of MnO₂ crystal structure on aerobic oxidation of 5-hydroxymethylfurfural to 2,5-furandicarboxylic acid, *J. Am. Chem. Soc.* 141 (2019) 890–900.
- [8] Y. Zhao, M. Cai, J. Xian, Y. Sun, G. Li, Recent advances in the electrocatalytic synthesis of 2,5-furandicarboxylic acid from 5-(hydroxymethyl)furfural, *J. Mater. Chem. A* 9 (2021) 20164–20183.
- [9] Y. Lu, C.L. Dong, Y.C. Huang, Y. Zou, Z. Liu, Y. Liu, Y. Li, N. He, J. Shi, S. Wang, Identifying the geometric site dependence of spinel oxides for the electrooxidation of 5-hydroxymethylfurfural, *Angew. Chem. Int. Ed.* 59 (2020) 19215–19221.
- [10] L. Xiong, J. Tang, Strategies and challenges on selectivity of photocatalytic oxidation of organic substances, *Adv. Energy Mater.* 11 (2021) 2003216.
- [11] I. Krivtsov, E.I. García-López, G. Marci, L. Palmisano, Z. Amghouz, J.R. García, S. Ordóñez, E. Díaz, Selective photocatalytic oxidation of 5-hydroxymethyl-2-furfural to 2,5-furandicarboxyaldehyde in aqueous suspension of g-C₃N₄, *Appl. Catal. B: Environ.* 204 (2017) 430–439.
- [12] H. Zhang, Z. Feng, Y. Zhu, Y. Wu, T. Wu, Photocatalytic selective oxidation of biomass-derived 5-hydroxymethylfurfural to 2,5-diformylfuran on WO₃/g-C₃N₄ composite under irradiation of visible light, *J. Photochem. Photobiol. A* 371 (2019) 1–9.
- [13] A. Khan, M. Goepel, A. Kubas, D. Lomot, W. Lisowski, D. Lisovyskiy, A. Nowicka, J.C. Colmenares, R. Glaser, Selective oxidation of 5-hydroxymethylfurfural to 2,5-diformylfuran by visible light-driven photocatalysis over in situ substrate-sensitized titania, *ChemSusChem* 14 (2021) 1351–1362.
- [14] D.A. Giannakoudakis, V. Nair, A. Khan, E.A. Deliyanni, J.C. Colmenares, K. S. Triantafyllidis, Additive-free photo-assisted selective partial oxidation at ambient conditions of 5-hydroxymethylfurfural by manganese (IV) oxide nanorods, *Appl. Catal. B: Environ.* 256 (2019), 117803.
- [15] M. Zhang, Z. Yu, J. Xiong, R. Zhang, X. Liu, X. Lu, One-step hydrothermal synthesis of Cd₃In₂S₈(x+1.5y) for photocatalytic oxidation of biomass-derived 5-hydroxymethylfurfural to 2, 5-diformylfuran under ambient conditions, *Appl. Catal. B: Environ.* 300 (2022), 120738.
- [16] T. Xia, W. Gong, Y. Chen, M. Duan, J. Ma, X. Cui, Y. Dai, C. Gao, Y. Xiong, Sunlight-driven highly selective catalytic oxidation of 5-hydroxymethylfurfural towards tunable products, *Angew. Chem. Int. Ed.* 61 (2022), e202204225.
- [17] M. Zhang, Y. Zhang, L. Ye, Z. Yu, R. Liu, Y. Qiao, L. Sun, J. Cui, X. Lu, In situ fabrication Ti₃C₂F_x MXene/CdIn₂S₄ Schottky junction for photocatalytic oxidation of HMF to DFF under visible light, *Appl. Catal. B: Environ.* 330 (2023), 122635.
- [18] R. Yang, L. Mei, Y. Fan, Q. Zhang, R. Zhu, R. Amal, Z. Yin, Z. Zeng, ZnIn₂S₄-based photocatalysts for energy and environmental applications, *Small Methods* 5 (2021), e2100887.
- [19] X. Cai, Z. Zeng, Y. Liu, Z. Li, X. Gu, Y. Zhao, L. Mao, J. Zhang, Visible-light-driven water splitting by yolk-shelled ZnIn₂S₄-based heterostructure without noble-metal co-catalyst and sacrificial agent, *Appl. Catal. B: Environ.* 297 (2021), 120391.
- [20] P. Ru, E. Bi, Y. Zhang, Y. Wang, W. Kong, Y. Sha, W. Tang, P. Zhang, Y. Wu, W. Chen, X. Yang, H. Chen, L. Han, High electron affinity enables fast hole extraction for efficient flexible inverted perovskite solar cells, *Adv. Energy Mater.* 10 (2020) 1903487.
- [21] L. Chi, Z. Niu, X. Zhang, P. Yang, J. Liao, F. Gao, Z. Wu, K. Tang, M. Gao, Region- and sequence-controlled conjugated topological oligomers and polymers via boronate-tag assisted solution-phase strategy, *Nat. Commun.* 12 (2021) 5853.
- [22] J. Wang, D. Liu, Y. Zhu, S. Zhou, S. Guan, Supramolecular packing dominant photocatalytic oxidation and anticancer performance of PDI, *Appl. Catal. B: Environ.* 235 (2018) 251–261.
- [23] J. Yang, C. Mou, Ordered mesoporous Au/TiO₂ nanospheres for solvent-free visible-light-driven plasmonic oxidative coupling reactions of amines, *Appl. Catal. B: Environ.* 231 (2018) 283–291.
- [24] G. Kresse, J. Furthmüller, Efficient iterative schemes for ab initio total-energy calculations using a plane-wave basis set, *Phys. Rev. B* 54 (1996) 11169–11186.
- [25] G. Kresse, J. Furthmüller, Efficiency of ab-initio total energy calculation for metals and semiconductors using a plane-wave basis set, *Comput. Mater. Sci.* 6 (1996) 15–50.
- [26] S. Grimme, J. Antony, S. Ehrlich, H. Krieg, A consistent and accurate ab initio parametrization of density functional dispersion correction (DFT-D) for the 94 elements H–Pu, *J. Chem. Phys.* 132 (2010), 154104.
- [27] P.E. Blöchl, Projector augmented-wave method, *Phys. Rev. B* 50 (1994) 17953–17979.
- [28] J.P. Perdew, K. Burke, M. Ernzerhof, Generalized gradient approximation made simple, *Phys. Rev. Lett.* 77 (1996) 3865–3868.
- [29] T. Sun, J. Song, J. Jia, X. Li, X. Sun, Real roles of perylenetetracarboxylic diimide for enhancing photocatalytic H₂-production, *Nano Energy* 26 (2016) 83–89.
- [30] E. Amdeha, R.S. Mohamed, A.S. Dhmees, Sonochemical assisted preparation of ZnS–ZnO/MCM-41 based on blast furnace slag and electric arc furnace dust for Cr (VI) photoreduction, *Ceram. Int.* 47 (2021) 23014–23027.
- [31] L. Ye, Z. Li, Rapid microwave-assisted syntheses of reduced graphene oxide (RGO)/ZnIn₂S₄ microspheres as superior noble-metal-free photocatalyst for hydrogen evolutions under visible light, *Appl. Catal. B: Environ.* 160–161 (2014) 552–557.
- [32] X. Xu, Y. Su, Y. Dong, X. Luo, S. Wang, W. Zhou, R. Li, K.P. Homewood, X. Xia, Y. Gao, X. Chen, Designing and fabricating a CdS QDs/Bi₂MoO₆ monolayer S-scheme heterojunction for highly efficient photocatalytic C₂H₄ degradation under visible light, *J. Hazard. Mater.* 424 (2022), 127685.
- [33] J. Wang, W. Shi, D. Liu, Z. Zhang, Y. Zhu, D. Wang, Supramolecular organic nanofibers with highly efficient and stable visible light photooxidation performance, *Appl. Catal. B: Environ.* 202 (2017) 289–297.
- [34] Z. Xu, P. Li, N. Li, W. Wang, C. Guo, M. Shan, X. Qian, Constructing dense and hydrophilic forward osmosis membrane by cross-linking reaction of graphene quantum dots with monomers for enhanced selectivity and stability, *J. Colloid Interface Sci.* 589 (2021) 486–499.

- [35] J. Yang, H. Miao, W. Li, H. Li, Y. Zhu, Designed synthesis of a p-Ag₂S/n-PDI self-assembled supramolecular heterojunction for enhanced full-spectrum photocatalytic activity, *J. Mater. Chem. A* 7 (2019) 6482–6490.
- [36] Z. Zhang, X. Chen, H. Zhang, W. Liu, W. Zhu, Y. Zhu, A highly crystalline perylene imide polymer with the robust built-in electric field for efficient photocatalytic water oxidation, *Adv. Mater.* 32 (2020), e1907746.
- [37] S. Zhang, Y. Si, B. Li, L. Yang, W. Dai, S. Luo, Atomic-level and modulated interfaces of photocatalyst heterostructure constructed by external defect-induced strategy: a critical review, *Small* 17 (2021), e2004980.
- [38] C. Tan, M. Qi, Z. Tang, Y. Xu, Cocatalyst decorated ZnIn₂S₄ composites for cooperative alcohol conversion and H₂ evolution, *Appl. Catal. B: Environ.* 298 (2021), 120541.
- [39] J. Fang, Y. Chen, W. Wang, L. Fang, C. Lu, C. Zhu, J. Kou, Y. Ni, Z. Xu, Highly efficient photocatalytic hydrogen generation of g-C₃N₄-CdS sheets based on plasmon-enhanced triplet-triplet annihilation upconversion, *Appl. Catal. B: Environ.* 258 (2019), 117762.
- [40] L. Wang, B. Cheng, L. Zhang, J. Yu, In situ irradiated XPS investigation on S-scheme TiO₂@ZnIn₂S₄ photocatalyst for efficient photocatalytic CO₂ reduction, *Small* 17 (2021), e2103447.
- [41] Y. Zhu, L. Wang, Y. Liu, L. Shao, X. Xia, In-situ hydrogenation engineering of ZnIn₂S₄ for promoted visible-light water splitting, *Appl. Catal. B: Environ.* 241 (2019) 483–490.
- [42] X. Gao, T.T. Nguyen, X. Gong, X. Chen, Z. Song, W. Du, R. Chai, M. Guo, A composite material of vacuum heat-treated CQDs/Ce_{0.7}Zr_{0.3}O₂ with enhanced charge separation for efficient photocatalytic degradation, *Vacuum* 169 (2019), 108912.
- [43] D.A. Gonzalez-Casamachin, J. Rivera De la Rosa, C.J. Lucio-Ortiz, L. Sandoval-Rangel, C.D. García, Partial oxidation of 5-hydroxymethylfurfural to 2,5-furandicarboxylic acid using O₂ and a photocatalyst of a composite of ZnO/PPy under visible-light: electrochemical characterization and kinetic analysis, *Chem. Eng. J.* 393 (2020), 124699.
- [44] G. Feng, P. Cheng, W. Yan, M. Boronat, X. Li, Ji Su, J. Wang, Y. Li, A. Corma, R. Xu, J. Yu, Accelerated crystallization of zeolites via hydroxyl free radicals, *Science* 351 (6278) (2016) 1188–1191.
- [45] Y. Nosaka, A.Y. Nosaka, Generation and detection of reactive oxygen species in photocatalysis, *Chem. Rev.* 117 (2017) 11302–11336.
- [46] Z. Huang, N. Luo, C. Zhang, F. Wang, Radical generation and fate control for photocatalytic biomass conversion, *Nat. Rev. Chem.* 6 (2022) 197–214.
- [47] S. Pan, L. He, J. Peng, F. Qiu, Z. Lin, Chemical-bonding-directed hierarchical assembly of nanoribbon-shaped nanocomposites of gold nanorods and poly(3-hexylthiophene), *Angew. Chem. Int. Ed.* 55 (2016) 8686–8690.
- [48] X. Sun, X. Luo, X. Zhang, J. Xie, S. Jin, H. Wang, X. Zheng, X. Wu, Y. Xie, Enhanced superoxide generation on defective surfaces for selective photooxidation, *J. Am. Chem. Soc.* 141 (2019) 3797–3801.
- [49] M. Chen, K. Hagedorn, H. Gölfen, S. Polarz, Functional gradient inverse opal carbon monoliths with directional and multinary porosity, *Adv. Mater.* 29 (2017) 1603356.
- [50] X. Sheng, Z. Liu, R. Zeng, L. Chen, X. Feng, L. Jiang, Enhanced photocatalytic reaction at air-liquid-solid joint interfaces, *J. Am. Chem. Soc.* 139 (2017) 12402–12405.
- [51] Y. Xin, Y. Lu, C. Han, L. Ge, P. Qiu, Y. Li, S. Fang, Novel NiS cocatalyst decorating ultrathin 2D TiO₂ nanosheets with enhanced photocatalytic hydrogen evolution activity, *Mater. Res. Bull.* 87 (2017) 123–129.
- [52] P. Kong, H. Tan, T. Lei, J. Wang, W. Yan, R. Wang, E. Wacławik, Z. Zheng, Z. Li, Oxygen vacancies confined in conjugated polyimide for promoted visible-light photocatalytic oxidative coupling of amines, *Appl. Catal. B: Environ.* 272 (2020), 118964.
- [53] M. Fumanal, A. Ortega-Guerrero, K. Jablonka, B. Smit, I. Tavernelli, Charge separation and charge carrier mobility in photocatalytic metal-organic frameworks, *Adv. Funct. Mater.* 30 (2020) 2003792.
- [54] P. Río, P. Abril, J. López, M. Sodupe, A. Lledós, M. Ciriano, C. Tejel, Activating a peroxo ligand for C–O bond formation, *Angew. Chem. Int. Ed.* 58 (2019) 3037–3041.
- [55] Q. Zhi, W. Liu, R. Jiang, X. Zhan, Y. Jin, X. Chen, X. Yang, K. Wang, W. Cao, D. Qi, J. Jiang, Piperazine-linked metalphthalocyanine frameworks for highly efficient visible-light-driven H₂O₂ photosynthesis, *J. Am. Chem. Soc.* 144 (2022) 21328–21336.
- [56] Y. Zhang, Y. Huang, S.S. Zhu, Y.Y. Liu, X. Zhang, J.J. Wang, A. Braun, Covalent S–O bonding enables enhanced photoelectrochemical performance of Cu₂S/Fe₂O₃ heterojunction for water splitting, *Small* 17 (2021), e21003.